

Design and control of a collision-resilient aerial vehicle with an icosahedron tensegrity structure

Jiaming Zha, Xiangyu Wu, Ryan Dimick, and Mark W. Mueller

Abstract—We present the tensegrity aerial vehicle, a design of collision-resilient rotor robots with icosahedron tensegrity structures. The tensegrity aerial vehicles can withstand high-speed impacts and resume operation after collisions. To guide the design process of these aerial vehicles, we propose a model-based methodology that predicts the stresses in the structure with a dynamics simulation and selects components that can withstand the predicted stresses. Meanwhile, an autonomous re-orientation controller is created to help the tensegrity aerial vehicles resume flight after collisions. The re-orientation controller can rotate the vehicles from arbitrary orientations on the ground to ones easy for takeoff. With collision resilience and re-orientation ability, the tensegrity aerial vehicles can operate in cluttered environments without complex collision-avoidance strategies. Moreover, by adopting an inertial navigation strategy of replacing flight with short hops to mitigate the growth of state estimation error, the tensegrity aerial vehicles can conduct short-range operations without external sensors. These capabilities are validated by a test of an experimental tensegrity aerial vehicle operating with only onboard inertial sensors in a previously-unknown forest.

I. INTRODUCTION

Autonomous aerial vehicles are fragile robots because they are weight-sensitive, and any damage to propellers or electronics can lead to loss of flight ability. Methods to protect aerial vehicles fall into two categories: detecting and avoiding collisions, and/or preventing physical damage caused by collisions. Some recent work of the first category includes methods to detect obstacles through collecting environmental information with LiDARs [1] or depth cameras [2]. The aerial vehicles can then use the collected obstacle information to plan motions that avoid collisions. A survey summarizing recent development in collision avoidance technologies is in [3]. Methods of the second category, which this work belongs to, help aerial vehicles operate more safely in cluttered environments, where accidental collisions may occur due to imperfect sensing or control. In this paper, we present the tensegrity aerial vehicle, a design of collision-resilient rotor robots with icosahedron tensegrity structures. The tensegrity aerial vehicles can withstand high-speed impacts and resume operation after collisions. With these capabilities, they can safely operate in cluttered environments without complex collision-avoidance strategies.

A. Related work: collision-resilient aerial vehicles

Many collision-resilient aerial vehicle designs exist in the literature and two main approaches are used to creating them:

- 1) Protecting the vehicle with external structures like propeller guards [4], [5] or shells [6], [7], [8], [9], [10].
- 2) Increasing the energy absorption ability of vehicle parts like propellers and arms [11], [12].

Designs with the first approach use external structures to isolate the fragile parts of aerial vehicles from obstacles. For instance, spherical guards that can freely rotate around propellers are proposed in [4]. Besides protecting propellers, these spherical guards can act as wheels to help the robot move on the ground. Another example is a flying robot with an external spherical shell connected to a gimbal system [6]. The gimbal isolates the parts inside the shell from external moments and thus increases the robot's collision resilience. Resilient designs of the second approach rely on deformable parts that can absorb a large quantity of energy before breaking. For instance, a quadcopter frame with dual stiffness materials that stays rigid during flights, and turns soft to deform during collisions is proposed in [11]. Some designs use both approaches for additional collision resilience. For example, a quadcopter with both spring-loaded deformable arms and propeller guards is proposed in [13].

Collision resilience also brings new opportunities for motion planning for aerial vehicles. A collision-tolerant planner that uses additional information from collisions to increase the reliability of visual-inertial odometry is proposed in [14]. Meanwhile, collisions can be exploited as a method to rapidly change the direction of movement. For example, a mixed-integer optimization method is introduced to plan trajectories that can exploit collisions in [15] and a sampling-based method is proposed for collision-inclusive motion planning in [16]. By allowing collisions, these planners can plan motions in a larger state space, and thus can generate faster trajectories.

B. Related work: tensegrity structure

In recent years, the tensegrity structure has become popular for collision-resilient designs. A tensegrity structure is composed of rigid bodies suspended in a tension network, and an external load on the tensegrity will be distributed among structural members as tension and compression. Specifically, large stress concentrations caused by bending effects are avoided. Due to this structural advantage, the tensegrity structure has been proposed for applications like aircraft wings[17], landers [18], [19], [20], exploratory rovers [21], [22] and swarm robots for terrestrial exploration [23]. The structural advantage of tensegrities also makes them good fits for aerial robots. A theoretical investigation together with drop tests to compare different tensegrity shells is made in [24]. The report concludes

The authors are with the HiPeRLab, University of California, Berkeley, CA 94720, USA. {jiaming_zha, wuxiangyu, rdimick, mwm}@berkeley.edu

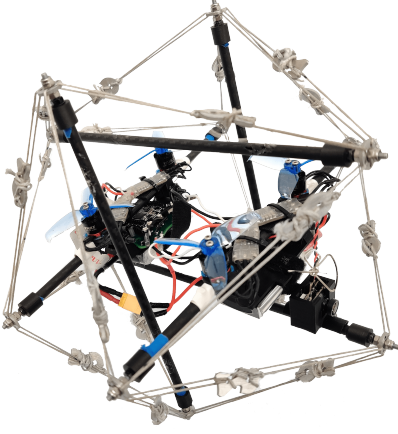


Figure 1. The icosahedron tensegrity aerial vehicle created with the proposed model-based design methodology. The length of each rod in the icosahedron tensegrity shell is 20cm. All electronics are directly mounted on the rods of the icosahedron tensegrity. It carries a wireless camera used for surveying the surroundings.

that for tensegrities of the same size, those made with lighter and stiffer material can survive higher drops in the test. In our prior work [25] we have presented a design of a quadcopter with a stiff tensegrity shell. Another example of an aerial robot with a tensegrity shell is the ‘Tensodrone’ [26], wherein a soft shell with springs is introduced. A self-morphing ‘Tensodrone’ is later presented as extension work in [27]. The soft tensegrity design helps increase collision resilience at the cost of larger vehicle size and vibration. We will discuss the difference between stiff and soft tensegrity shell designs in Section II.

C. Contribution: tensegrity aerial vehicle

In this paper, we present the tensegrity aerial vehicles, which are collision-resilient rotor robots in the form of quadcopters with stiff icosahedron tensegrity structures. These vehicles can take advantage of both the collision resilience of tensegrities and the mobility of quadcopters. Moreover, they can resume flight after collisions. To guide the design process of these vehicles, we propose a model-based methodology, which uses a dynamics simulation of collisions to predict the stresses in the structure and then selects structural components that can withstand the predicted stresses. Meanwhile, we create an autonomous re-orientation controller to help prepare the vehicles to take off again after collisions. Exploiting the sphere-like geometry of the icosahedron, the controller can rotate tensegrity aerial vehicles from arbitrary orientations on the ground to ones easy for takeoff. With collision resilience and re-orientation ability, tensegrity aerial vehicles can operate in cluttered environments without complex collision-avoidance strategies. Moreover, we further extend the vehicles’ ability by adopting the inertial navigation method in [28], which enables them to perform short-range autonomous operations without external sensing. The resulting vehicles can thus serve as field robots and work on challenging tasks like traversing through a cluttered corridor filled with smoke to search for survivors during firefighting.

The contribution of this work is as follows. First, we present a model-based methodology to design collision-resilient tensegrity vehicles with a dynamics simulation tool that we have open-sourced. Second, we propose a control strategy to re-orient tensegrity aerial vehicles from arbitrary orientations on the ground to help them resume flight after collisions. Third, we present an experimental vehicle designed with the proposed methodology (Fig. 1) and validate the vehicle’s ability to survive collisions, resume flight after collisions and conduct short-range autonomous operations without external sensors in a previously-unknown forest environment. This paper is an evolved paper based on prior work [25], with the following extensions:

- 1) presenting a new model-based design methodology with dynamics simulation;
- 2) demonstrating the structural advantage of tensegrity over common protection shells like propeller guards;
- 3) presenting a new stiff tensegrity drone design whose rigid members are not rigidly connected. The new design helps the vehicle to achieve higher collision resilience by reducing stress concentration in the system;
- 4) proposing a new re-orientation controller with an optimization-based method to convert torque command to thrust command, in order to take full advantage of the vehicle’s limited thrust generation ability;
- 5) adopting the inertial navigation method in [28] so that the tensegrity vehicle can perform short-range autonomous operations without external sensing;
- 6) validating the vehicle’s abilities with additional field experiments in a forest environment previously-unknown to the experimental vehicle.

The source code of the tensegrity aerial vehicle simulation and structural advantage analysis is available at: github.com/muellerlab/TensegrityAerialVehicleCollisionSim.

II. DESIGN OF THE TENSEGRITY SHELL

In this section, we motivate the idea of protecting a quadcopter with a stiff icosahedron tensegrity shell, introduce the methodology used to design the tensegrity with stress analysis based on a dynamics simulation, and showcase the structural advantage of the proposed idea.

We choose to design the tensegrity aerial vehicle in the form of a quadcopter because the abilities to hover and to vertically take off and land make operation easier in cluttered environments. The differential flatness of the quadcopter also allows us to quickly plan trajectories and check their feasibility [29]. Meanwhile, we choose to protect the quadcopter with a 6-rod orthogonal icosahedron [30] tensegrity, because its shape is close to a sphere and can provide protection against collisions from all directions with the least amount of rods.

To protect the quadcopter from damage, the tensegrity shell should not break during collisions and the deformation of the shell should be small so that external obstacles do not contact parts such as propellers or sensitive electronics. Therefore, the success of the tensegrity design depends on choosing components (rods and strings) with suitable stiffness

and strength. We desire stiff components with little flexibility for two reasons. First, the deformation of a stiff shell during collisions is small, so the shell needs little buffer space to prevent propellers and electronics from being exposed. Thus, the tensegrity can be smaller in size and this helps the vehicle to fit through narrow gaps. Second, a stiff tensegrity experiences less disruptive vibration in the system, which leads to less disturbance during flights. Meanwhile, we prefer light components as they help retain the agility and flight time of the aerial vehicle. In the following subsection, we detail the process to determine if certain components can meet the tensegrity design requirements.

A. Stress analysis with dynamics simulation

To predict if a tensegrity aerial vehicle can survive a collision, we simulate the dynamics of the tensegrity structure during the collision and predict the stress in the structure with the simulation result. Compared to the static stress analysis method we proposed in [25], this dynamics method has two advantages. First, it takes the deformation of the tensegrity into account and captures the transient effects during stress propagation. Second, it considers the stress concentration caused by the mass of the quadcopter mounted on the tensegrity rods. These advantages lead to a more accurate stress estimate and allow us to easily verify if the tensegrity design meets the deformation criteria.

We simplify the tensegrity vehicle as point masses suspended in a stress network, as shown in Fig. 2a. We define a *tensegrity node* as the point connecting a rod to strings. An icosahedron tensegrity has 12 nodes and each node is a point mass representing the mass of fasteners at the position of the node, as well as half of the rod and the strings connected to the node. Each tensegrity node is connected to a rod and four strings modeled as massless linear spring-damper pairs, shown in Fig. 2b. Similarly, we represent the quadcopter with four *quadcopter nodes* mounted on a pair of parallel rods of the tensegrity shell. Each quadcopter node is a point mass representing the propeller and motor mounted at its position,

as well as a quarter of the batteries and the electronics. A pair of quadcopter nodes split the *full-length rod* on which they are mounted into three pieces of *short rods*. We model each connection between short rods as a torsional spring-damper pair, as illustrated in Fig. 2c. Notice that our model allows relative rotation between short rods rather than treating the rod holding the quadcopter mass as a single rigid piece without any bending. This approach helps us capture the transient stress concentration effect caused by the quadcopter mass.

We denote the nodes in the system as n_i , where $i = 1, \dots, 12$ for the tensegrity nodes and $i = 13, \dots, 16$ for the quadcopter nodes. Let \mathbf{x}_i be the position of node i . For clarity and consistency, we denote variables related to rods with superscript r and variables related to strings with superscript s . The connectivity of the nodes can then be represented with indicator variables $N_{i,j}^r$ and $N_{i,j}^s$:

$$N_{i,j}^r = \begin{cases} 1, & \text{if a rod connects } n_i \text{ and } n_j \\ 0, & \text{otherwise} \end{cases} \quad (1)$$

$$N_{i,j}^s = \begin{cases} 1, & \text{if a string connects } n_i \text{ and } n_j \\ 0, & \text{otherwise} \end{cases} \quad (2)$$

We further define $T_{i,j}$ and $C_{i,j}$ respectively as the value of the tensile force in string and compression force in rod connecting node n_i and n_j . They can be calculated from Hooke's law, with a special modification that strings generate no force when compressed:

$$T_{i,j} = \begin{cases} N_{i,j}^s K^s \delta L_{i,j} = N_{i,j}^s K^s (L_{i,j} - L^s), & \text{if } L_{i,j} \geq L^s \\ 0, & \text{otherwise} \end{cases} \quad (3)$$

$$C_{i,j} = N_{i,j}^r K_{i,j}^r \delta L_{i,j} = N_{i,j}^r K_{i,j}^r (L_{i,j}^r - L_{i,j}) \quad (4)$$

where K^s is the spring constant of the string and $K_{i,j}^r$ is the spring constant of the rod connecting n_i and n_j . As we are modeling both full-length rods and short rods, we use subscripts i and j to identify the nodes linked by the rod to differentiate, following the convention illustrated in Fig. 2c. $L_{i,j} = \|\mathbf{x}_i - \mathbf{x}_j\|$ is the distance between node n_i and n_j . $\delta L_{i,j}$ is the length deformation, which is the difference between $L_{i,j}$, the length under external load, and L^s or $L_{i,j}^r$, the original string or rod length without deformation. Notice that due to the existence of possible self-stress (also known as pre-tension) in the icosahedron tensegrity [31], tensegrity components may be deformed even when the tensegrity is under no external load.

In addition to the tensile and compression forces, there exist linear damping forces which impede relative linear motion between nodes. We assume that these forces are aligned with the strings and rods, and the value is proportional to the relative velocity of the nodes:

$$D_{i,j} = (N_{i,j}^s + N_{i,j}^r) c (\dot{\mathbf{x}}_j - \dot{\mathbf{x}}_i)^T \mathbf{e}_{i,j} \quad (5)$$

where $\mathbf{e}_{i,j} \in \mathbb{R}^3$ is the unit vector pointing from n_i to n_j and c is the linear damping coefficient.

Additionally, for the connections between short rods, which are modeled as torsional spring-damper pairs and shown in Fig. 2c, we assume the spring moment is proportional to the

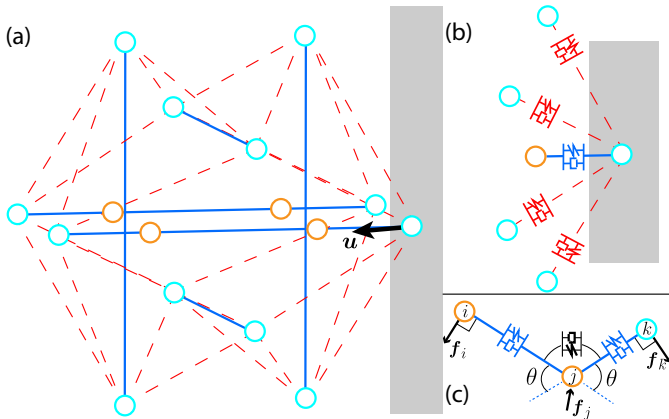


Figure 2. (a) The tensegrity vehicle is simplified as point masses in a stress network. Cyan spheres represent tensegrity nodes whereas orange spheres represent quadcopter nodes. (b) Strings and rods are modeled as massless spring-damper pairs. (c) Connections between two short rods are modeled as torsional spring-damper pairs.

angle between the neighboring rod and the damping moment is proportional to the angular velocity:

$$M_j = \begin{cases} \kappa_j \theta + d\dot{\theta}, & \text{if } n_j \text{ connects two short rods} \\ 0, & \text{otherwise} \end{cases} \quad (6)$$

where κ_j is the torsional spring constant and d is the torsional damping constant at n_j . For pure bending of a rod, the radius of curvature is proportional to the product of Young's modulus E^r and second moment of area I^r [32]. Notice that the bending angle is the ratio between the rod length and the radius of curvature. We can thus compute the bending stiffness as:

$$\kappa_j = \frac{E^r I^r}{L_{i,j}} \quad (7)$$

As the mass of rods is assumed to be lumped at the nodes, the moment is equivalent to forces acting on nodes at the ends of the rods in orthogonal directions and a balancing force acting on the joint:

$$\mathbf{f}_i = \frac{M_j}{L_{i,j}} \mathbf{e}_{\perp ji} \quad (8)$$

$$\mathbf{f}_k = \frac{M_j}{L_{j,k}} \mathbf{e}_{\perp jk} \quad (9)$$

$$\mathbf{f}_j = -(\mathbf{f}_k + \mathbf{f}_i) \quad (10)$$

where $\mathbf{e}_{\perp ji}$ and $\mathbf{e}_{\perp jk}$ are respectively unit vectors perpendicular to $\mathbf{e}_{j,i}$ and $\mathbf{e}_{j,k}$, pointing in the directions that would decrease the joint angle θ .

Let \mathbf{f}_{bi} represent the force due to bending on node n_i and let \mathbf{u}_i represent the external force acting on n_i . We use a method similar to [33] and derive the equations of motion of the system with Newton's second law for each node i :

$$\mathbf{f}_{bi} + \mathbf{u}_i + \sum_j (T_{i,j} - C_{i,j} + D_{i,j}) \mathbf{e}_{i,j} = m_i \cdot \ddot{\mathbf{x}}_i \quad (11)$$

where m_i is the mass of n_i .

To simulate the dynamics of the system, we need to specify the external force acting on the tensegrity during the collision process. One way to estimate the force is to simplify the obstacle as a stiff linear spring so that the magnitude of the force acting on the tensegrity is proportional to the distance that the tensegrity node has penetrated the obstacle:

$$\|\mathbf{u}_i\| = k_o p_i \quad (12)$$

where k_o is the stiffness of the obstacle and p_i is the penetration distance of n_i . Studies on the stiffness of common obstacles like concrete walls can be found in the literature [34]. We assume the surface of the obstacle is frictionless, so reaction forces point out of the obstacle and are normal to the obstacle surface.

We simulate the dynamics system described by Eq. (11) by providing the initial position and velocity of the nodes and numerically solving the corresponding initial value problem. The solution gives us positions of nodes over the simulated time, and we can then extract the tensile and compressive forces, as well as bending moment from these positions. The

axial stress in the string or rod connecting n_i and n_j can then be expressed as a function of simulation time:

$$\sigma_{i,j}^s(t) = \frac{T_{i,j}(t)}{A^s}, \quad \sigma_{i,j}^r(t) = \frac{C_{i,j}(t)}{A^r} \quad (13)$$

where $\sigma_{i,j}^s$ and $\sigma_{i,j}^r$ are axial stress in corresponding strings and rods respectively. A^s and A^r are cross sectional areas of strings and rods.

Furthermore, at the connection between two short rods, we use the beam bending formula in [35] and compute the stress caused by bending at the rod surface:

$$\sigma_j^b(t) = \frac{M_j(t)r}{I^r} \quad (14)$$

where r is the radius of rod. Thus, the maximum stress at the node connecting two short rods will be the sum of the bending stress at the rod surface and the maximum axial stress in the rods connected to it:

$$\sigma_j^r(t) = \sigma_j^b(t) + \max_i(\sigma_{i,j}^r(t)) \quad (15)$$

We can then use the computed stress information to check if the candidate components meet the design objectives. First, the stresses in the strings have to be smaller than their yielding strength σ^{sy} , with a factor of safety for string η^s :

$$\forall i, j, t \quad \eta^s \sigma_{i,j}^s(t) < \sigma^{sy} \quad (16)$$

Second, the axial stress in each rod should be smaller than its yielding strength σ^{ry} and critical buckling strength $\sigma_{i,j}^{rb}$ with a factor of safety for rod η^r :

$$\forall i, j, t \quad \eta^r \sigma_{i,j}^r(t) < \min(\sigma^{ry}, \sigma_{i,j}^{rb}) \quad (17)$$

Here the rod's critical buckling strength can be approximated with Euler's buckling theory:

$$\sigma_{i,j}^{rb} = \frac{\pi^2 E^r I^r}{A^r (L_{i,j}^r)^2} \quad (18)$$

Third, the stresses at the nodes connecting two short rods should also be smaller than the rod yielding strength with the factor of safety for rod:

$$\forall j, t \quad \eta^r \sigma_j^r(t) < \sigma^{ry} \quad (19)$$

In addition to the stress condition, we need to check that the propeller and electronics are not exposed during collisions. We can compute the distances between the tensegrity surface and the quadcopter nodes and ensure they are longer than a given threshold. The dynamics simulation, together with the stress check and the no-exposure check, allows us to quickly rule out candidate components that fail to meet the design objectives without physically constructing and testing the tensegrity structures.

B. Structural advantage of the icosahedron tensegrity

External loads on an icosahedron tensegrity shell will be dispersed among its structural members as tension and compression, and large stress concentrations caused by bending effects are avoided. As a result, an icosahedron tensegrity shell can better survive collisions than common protective structures

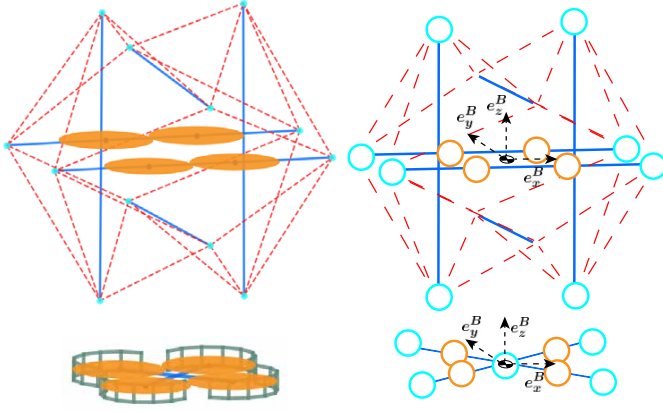


Figure 3. Left: illustration of the two collision-resilient vehicle designs used for comparison. The top vehicle has a tensegrity shell whereas the bottom vehicle uses a propeller guard. Both vehicles have the smallest possible protection structure to host quadcopters with propellers of the same size. Right: we model both vehicles as point masses suspended in structures made with massless rods and/or strings modeled as massless spring-damper pairs and joints as torsional spring-damper pairs. We describe the vehicle's body-fixed frame with a set of three axes orthogonal to each other: e_x^B , e_y^B and e_z^B . Notice that for the tensegrity aerial vehicle, the quadcopter nodes are on the rods parallel with the e_x^B axis.

like propeller guards. To show this structural advantage, we conduct a Monte Carlo study of simulated wall-collision experiments and compare the maximum stresses in two aerial vehicle designs, one with an icosahedron tensegrity shell and the other with a planar propeller guard.

Both designs for our simulated experiments host a quadcopter with total mass m_q and propeller diameter d . The first design has the smallest tensegrity shell that can wrap the propellers fully inside the shell without propeller overlapping, whereas the second design has the smallest quadcopter frame that can host the propellers and then protect it with a propeller guard. For simplicity, we depict the vehicles' body-fixed frames with three axes (e_x^B , e_y^B , e_z^B) orthogonal to each other, as illustrated in Fig. 3. We assume that both the tensegrity shell and the propeller guard frame have the same mass m_s and both structures are made with solid cylindrical rods of the same material, so they have the same density ρ^r and Young's modulus E^r . To fully define the tensegrity structure, we in addition specify γ_m , the ratio between the total mass of rods and total mass of strings in the tensegrity shell, and F_s , the pre-tension force in strings. It is worth noting that our analysis shows the maximum stress during a collision is insensitive to these parameters. Meanwhile, similar to the tensegrity model, the quadcopter with propeller guard is simplified as mass points in a network of rods modeled as massless linear spring-damper pairs connected by joints modeled as torsional springs and dampers. Notice that there is a minor change in the model: for the joint connecting two perpendicular rods, the rest angle corresponding to zero moment is $\frac{\pi}{2}$. Moreover, for both the tensegrity vehicle and the propeller-guard vehicle, we assume the dampers will make the corresponding systems, including the spring-damper pair and their directly-connected nodes, critically damped.

In our simulated experiments, we consider a wall with

stiffness k_o . Before the collision, the tensegrity aerial vehicle and the propeller guard vehicle move perpendicularly toward the wall with a speed v . Both vehicles do not rotate before collisions. We conduct the Monte Carlo study by simulating 2000 experiments with different random collision orientations generated with the following steps. First, we randomly sample points with a uniform distribution on the surface of a unit sphere attached to the vehicle's body-fixed frame. Then, we compute the collision orientation as the rotation which maps the vector pointing from the origin to the sampled point in the body-fixed frame to a vector pointing perpendicularly to the wall in an inertial frame attached to the wall. Due to the symmetry of both vehicles, we only need to study collision orientations corresponding to nodes sampled in a single octant (one of the eight divisions of the Euclidean space separated by the three orthogonal axes) of the sphere surface.

The Monte Carlo study are conducted with key parameters in Table I. The parameters correspond to a tensegrity shell made with carbon fiber rods and braided nylon string. Additionally, we choose $F_s = 20\text{N}$, which corresponds to a stiff shell without large pre-tension stress in the system.

Table I
KEY PARAMETERS USED IN THE COMPARISON SIMULATION EXAMPLE

Parameter	Value
total structure mass	$m_s = 50\text{g}$
total quadcopter mass	$m_q = 250\text{g}$
string pre-tension	$F^s = 20\text{N}$
rod-string mass ratio	$\gamma_m = 20$
rod density	$\rho^r = 2000\text{kg/m}^3$
string density	$\rho^s = 1150\text{kg/m}^3$
rod Young's modulus	$E^r = 3.2 \times 10^{10}\text{Pa}$
string Young's modulus	$E^s = 4.1 \times 10^9\text{Pa}$
diameter of 2.5-inch propellers	$d = 63\text{mm}$
wall stiffness	$k_o = 4.7 \times 10^7\text{N/m}$
initial speed before collision	$v = 5\text{m/s}$

The result of the Monte Carlo study is visualized in Fig. 4 in terms of scattered plots showing the maximum stress observed in the vehicles during collisions and a contour plot showing the ratio of the maximum stress in the propeller guard to the maximum stress in the tensegrity. The result indicates that the tensegrity holds a structural advantage over the propeller-guard for collision resilience. Among the 2000 simulated experiments, the mean of the maximum stress in tensegrity is 34.36MPa, whereas the mean of the maximum stress in propeller-guard is 100.47MPa. For 80% of the samples, the maximum stress in the tensegrity vehicle is smaller than half of that in the propeller-guard vehicle. On the other hand, the propeller-guard vehicle experiences a smaller maximum stress than the propeller-guard in only 2.7% of the case. It is also worth noting that the tensegrity gets the worst stress when the rods holding the quadcopter collide perpendicularly with the wall. In such cases, the deformation in tensegrity is limited and the load is not well-distributed through the structure.

In addition, we have investigated the structural advantage of the icosahedron tensegrity for vehicles of various scales. Specifically, we linearly scale all length-related parameters, cubically scale all mass and force-related parameters, and leave all parameters related to ratios or material characteristics

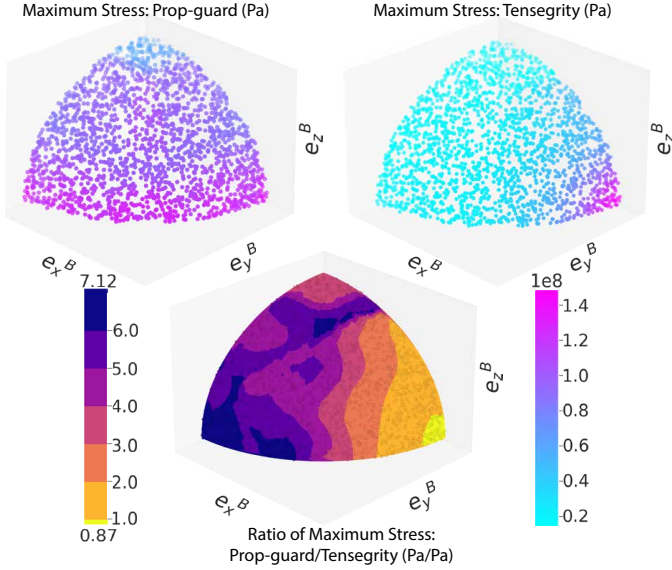


Figure 4. Visualization of the Monte Carlo study result. The positions of the points correspond to the collision orientation. Top left: scatter plot of the maximum stress in propeller guard during collisions. Top right: scatter plot of the maximum stress in tensegrity. Bottom: the ratio of the maximum stress in propeller guard to that in tensegrity. The color on the surface is interpolated from the scattered simulated experiment data points.

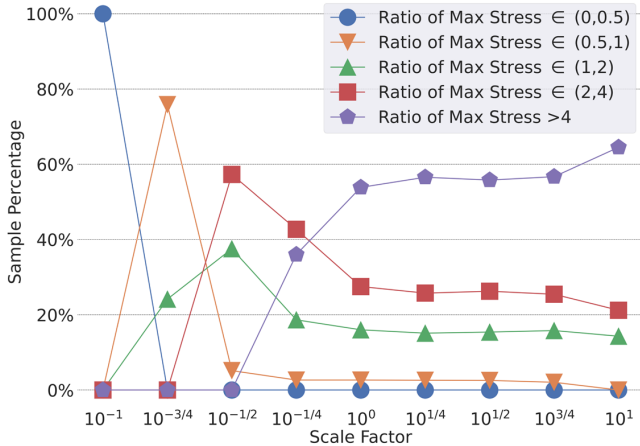


Figure 5. The figure demonstrates the structural advantage of the icosahedron tensegrity over the propeller guard for vehicles of various scales. The horizontal axis is the scale factor, whereas the vertical axis shows the percentage of the simulated experiments whose maximum stress ratio lies in the range indicated by plot legends. We see that as the scale factor increases, more samples move from the bins with small ratios (circle and triangle) to the bins with large ratios (squares and pentagons), suggesting that the structural advantage of the tensegrity becomes more salient as the vehicle scales up.

unchanged in Table. I. We then conduct the same Monte Carlo analysis for the scaled tensegrity aerial vehicle and propeller-guard vehicle and record the ratio of maximum stresses. The result of the analysis is plotted in Fig. 5. From the graph, we observe that the relative collision resilience of the icosahedron tensegrity increases as the vehicle scales up. The trend is related to the characteristic of the tensegrity structure. As the propeller guard gets larger, bending becomes the salient resource of stress due to the increase of the moment arm length. Meanwhile, the tensegrity shell can avoid large stress

concentration caused by the bending effects. As a result, as the vehicles scale up, the maximum stress in the tensegrity shell grows slower than that in the propeller guard. From the scaling analysis, we conclude that the icosahedron tensegrity is a more desirable collision-resilient structure for large-scale aerial vehicle designs.

III. DYNAMICS MODEL AND CONTROL OF TENSEGRITY AERIAL VEHICLES

In this section, we introduce the models used to describe the motions of the tensegrity aerial vehicles and the controllers used to regulate them. The tensegrity aerial vehicles mainly conduct two types of motions. When airborne, they use a flight controller and fly like normal quadcopters. When on the ground, the tensegrity aerial vehicles use a re-orientation controller to rotate themselves. The objective of re-orientation is to change the orientation from arbitrary starts to ones with propellers pointing upward, to prepare for takeoff. In our previous work [25], we reused the flight attitude controller for re-orientation. In this section, we will introduce a new re-orientation controller which offsets the gravitational torque and uses a new optimization-based thrust converter. The new controller optimizes the vehicle's re-orientation capability under the constraint of thrust generation authority and thus makes the re-orientation process more reliable.

A. System model

We illustrate the model used to describe the dynamics of the tensegrity aerial vehicle with Fig. 6. We assume that the external forces and torques acting on the vehicle include the weight of the vehicle, the thrust and torque generated by the propellers, and the forces due to contact with surrounding environments. When the vehicle is flying and not in contact with its surroundings, the contact forces are zero and the model reduces to a regular near-hover quadcopter flight model. We define the attitude of the vehicle \mathbf{R} as a $\mathbb{R}^{3 \times 3}$ rotation matrix

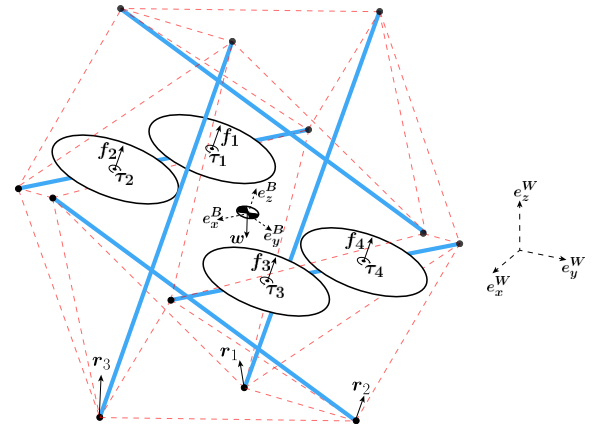


Figure 6. The figure illustrates the dynamics model of the tensegrity aerial vehicle. w denotes the weight. f_i and τ_i , where $i = 1, 2, 3, 4$, represent the forces and yaw torques generated by the propellers. r_j , where $j = 1, 2, 3 \dots$ denotes the contact forces acting on the vehicle. In this figure, three bottom nodes of the tensegrity shell are in contact with the ground. \mathbf{W} denotes the world frame fixed to the ground and \mathbf{B} denotes the vehicle's body-fixed frame.

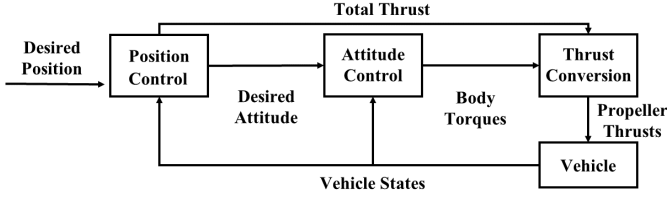


Figure 7. Structure of the flight controller used when the vehicle is airborne.

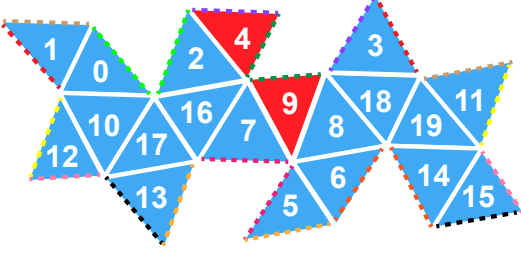


Figure 8. Faces of an unfolded icosahedron tensegrity. The tensegrity can take off when face 4 or 9 is contacting the ground. Dashed lines with the same color indicate overlapped edges when the tensegrity is folded back.

mapping a \mathbb{R}^3 vector in the body-fixed frame B to the world frame W , which we assume is fixed to the ground and is an inertial frame, i.e. $v^W = Rv^B$.

B. Flight controller

A standard quadcopter controller with a cascaded structure is used for flights. A position controller outputs the desired total thrust and thrust direction, whereas an attitude controller computes the desired torques. Finally, a linear thrust converter maps the total thrust and the body torque commands to per-propeller thrust commands. The structure of the controller is depicted in Fig. 7 and more details can be found in [25].

C. Re-orientation strategy

To help the tensegrity aerial vehicles resume flight after collisions, we create a re-orientation controller that can rotate the vehicles from arbitrary orientations to ones easy for takeoff. An icosahedron tensegrity has twenty faces and we define that two faces are neighboring if they share two nodes. We assume the tensegrity vehicle is on flat ground and denote the contact face as F_i if the i^{th} face of the tensegrity is contacting the ground. Fig. 8 illustrates an unfolded icosahedron and helps visualize the neighboring relationship of the tensegrity faces. When face 4 or 9 (the highlighted ones) contacts the ground, propellers will point upward, so the tensegrity vehicle is ready to take off. Thus, the goal of the re-orientation controller is to rotate the tensegrity aerial vehicles so that face 4 or 9 becomes the contact face.

The re-orientation controller uses a strategy that divides the task into a series of rotations between neighboring tensegrity faces. The strategy has two advantages. First, each rotation between neighboring faces is easy to model. Rotation axes are lines shared by neighboring faces and the total rotation angle comes directly from the icosahedron shape. Second,

the strategy reduces the problem into a finite state machine and makes the process more robust. If a rotation fails and the vehicle arrives at a state with an unexpected contact face, the controller can re-plan the path and proceed with the task.

The procedure to find re-orientation paths includes two steps. First, we create a connection graph whose nodes are the 20 contact faces and whose directed edges connecting the nodes represent feasible transitions between neighboring faces. A transition is deemed feasible if there exists a set of thrusts that can drive the vehicle leaving its starting face without sliding on the ground. If the graph is fully connected, the corresponding tensegrity vehicle can re-orient to any contact face. If the graph has disconnected nodes, the vehicle will get stuck and the re-orientation will fail. This normally happens when the torque generated by the propellers is too weak to offset the gravitational torque. A vehicle design update with stronger motors or longer arms is needed to solve this problem. In the second step, we can search from the generated connection graph for the shortest routes from a given starting face to one of the two goal faces. An example procedure of generating the re-orientation path for an experimental tensegrity aerial vehicle can be found in Section. IV.B.

D. Reference rotation trajectory for re-orientation

For each re-orientation step, the controller identifies the rotation needed for face change, generates a reference rotation trajectory, and then tracks the generated trajectory.

We use Fig. 9 to illustrate a rotation between neighboring faces. We denote F_a as the start face and F_b as the target neighboring face. We denote n_r as the rotation point about which we analyze the rotation, s_r as the rotation axis in the body-fixed frame and Θ_r as the rotation angle.

We choose to use a two-piece trajectory, which accelerates from stationary to the maximum angular velocity for the first half of the time and then decelerates to stop for the second half. The magnitude of angular acceleration stays the same throughout the process, except that the direction flips at the middle time of the duration. We choose this trajectory because the reference angular acceleration, which determines the aggressiveness, can be easily tuned by adjusting the total trajectory time T . Notice that the total rotation angle Θ_r

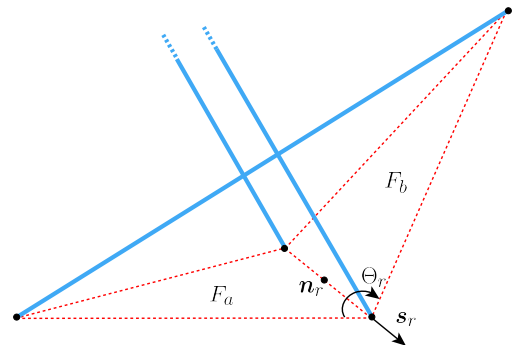


Figure 9. Rotation between neighboring contact faces. The tensegrity is rotating from face F_a to its neighbor face F_b . We can describe the rotation about rotation point n_r with a rotation axis s_r and a total rotation angle Θ_r .

is a constant. So, the magnitude of the reference angular acceleration only depends on T :

$$||\ddot{\Theta}_{ref}|| = \frac{4\Theta_r}{T^2} \quad (20)$$

At a given time t , we can express the reference state with a reference rotation vector Θ_{ref} , a reference angular velocity vector $\dot{\Theta}_{ref}$ and a reference angular acceleration vector $\ddot{\Theta}_{ref}$. All three vectors point along the rotation axis s_r . Moreover, we can find reference attitude from the reference rotation angle:

$$R_{ref}(t) = R_s f_{Rv}(\Theta_{ref}(t)) \quad (21)$$

where R_s is the attitude of the vehicle before the start of rotation and $f_{Rv}(\cdot)$ converts a rotation from rotation vector representation to its corresponding rotation matrix.

E. Tracking controller for re-orientation

To track the reference trajectory, we design a controller which generates a desired angular acceleration reducing the error as a second-order system:

$$\ddot{\Theta}_d = \ddot{\Theta}_{ref} + 2\zeta_r\omega_r(\dot{\Theta}_{ref} - \dot{\omega}) + \omega_r^2(\delta_r) \quad (22)$$

where ζ_r is the desired damping ratio, ω_r is the desired natural frequency of the rotation and $\dot{\omega}$ is the angular velocity reading from the rate gyroscope. δ_r is the attitude error represented as a rotation vector in the body-fixed frame and is computed as:

$$\delta_r = f_{vR}(R^{-1}R_{ref}) \quad (23)$$

where $f_{vR}(\cdot)$ converts a rotation matrix to a rotation vector.

The total desired torque command to track the trajectory can then be computed as the sum of the gravity torque offset and the torque to track the reference trajectory:

$$\tau_d = I_r \ddot{\Theta}_d - \tau_g \quad (24)$$

where I_r is the mass moment of inertia of the tensegrity aerial vehicle with respect to the rotation point. τ_g is the gravitational torque offset and can be computed as the cross product between the vector of gravity and the vector pointing from rotation point to the center of mass.

Next, we convert the torque command to per-propeller thrust command that the vehicle can directly implement. Notice that there exists a linear mapping from the thrusts to the torques generated by propellers:

$$\tau_p = M_r f \quad (25)$$

Here $f \in \mathbb{R}^4$ is a vector representing four propeller thrusts. Meanwhile, $M_r \in \mathbb{R}^{3 \times 4}$ is the mapping matrix and each of its columns can be found as:

$$m_{r,i} = S(p_i - n_r) e_z^B + (-1)^i \kappa e_z^B \quad (26)$$

where p_i is the position of the i^{th} propeller in body-fixed frame and κ is the propeller's yaw torque constant. $S(\cdot)$ maps a \mathbb{R}^3 vector to a corresponding $\mathbb{R}^{3 \times 3}$ skew-symmetrical matrix. A left multiplication with this skew-symmetrical matrix is equivalent to a cross product with the original vector.

However, the matrix M_r is not invertible. As a result, the reverse mapping from torque to thrust is not unique. Moreover,

as the range of thrusts is constrained by the physical limits of the motors and the propellers, we also need to take saturation into account. We choose to find thrust commands by solving the following optimization problems. When no thrusts are saturated and the exact desired torque can be generated, we command thrusts that minimize the norm of the thrust vector:

$$\begin{aligned} \min_f & ||f|| \\ \text{s.t. } & M_r f = \tau_d \\ & f_{min} \leq f_i \leq f_{max} \end{aligned} \quad (27)$$

where f_i denotes the thrust command for the i^{th} propeller.

When problem (27) is infeasible and therefore force saturation is unavoidable, we solve for a set of feasible thrusts that minimize the error norm between the desired torque and the torque to be generated:

$$\begin{aligned} \min_f & ||M_r f - \tau_d|| \\ \text{s.t. } & f_{min} \leq f_i \leq f_{max} \end{aligned} \quad (28)$$

Notice that both optimization problem (27) and (28) are of relatively low dimension. As a result, they can be solved in real time, even on embedded systems with limited computation power, via tools like CVXGEN [36]. A 3D graph representing the thrust mapping for an example rotation problem and demonstrating the advantage of the optimization-based thrust converter over the traditional pseudoinverse-clipping method can be found in Section. IV.B.

IV. EXPERIMENTAL VALIDATION

In this section, we present the resulting experimental tensegrity aerial vehicle designed with the methodology presented in Section. II, as well as the experiments to validate the vehicle's collision resilience and its ability to resume operation after collisions. In addition, we present a test of the experimental vehicle autonomously moving toward a goal in a previously-unknown forest, to demonstrate the vehicle's ability to conduct autonomous short-range operation with only onboard inertial sensors in a cluttered environment. The video attachment showing all experiments is available at: youtu.be/wPsXKjY5a4Y.

A. Experimental vehicle

An experimental vehicle is created to validate the abilities of the tensegrity aerial vehicles. A picture of the experimental vehicle is shown in Fig. 1. We choose to design an icosahedron tensegrity with 20mm rods. A tensegrity shell of this size can host a micro-scale quadcopter and camera inside while still easily fitting through narrow gaps between obstacles. We also choose to protect against collisions at a target operation speed of 6m/s. We use the design methodology in Section. II to screen if certain candidate rods or strings can be used to build the tensegrity shell. Among all possible candidates satisfying the design requirements, carbon fiber rods with 6mm outer diameter and braided nylon string are selected based on weight, price and availability. The total mass of the vehicle with a 30g camera payload is 315g. The maximum total thrust

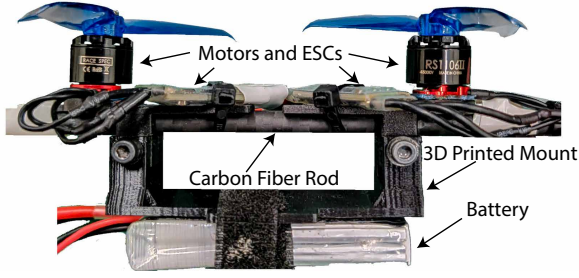


Figure 10. Side-view of the tensegrity vehicle. Each horizontal rod has a battery and a pair of motors and ESCs attached to it.

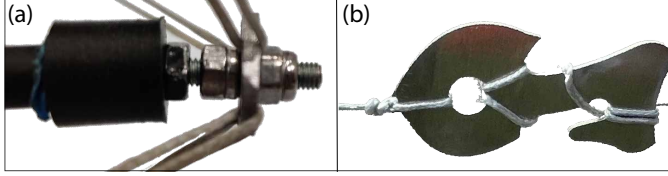


Figure 11. Components of incremental tensioning methods: (a) expanding end cap with washer for string routing and (b) tensioning hook.

of the vehicle is 8.5N, which leads to a 2.75:1 thrust-to-weight ratio. The mass breakdown of the vehicle is as follows.

Shell	Batteries	Electronics	Motors	Camera
80g	75g	50g	80g	30g

The resulting vehicle has no flat frame that is commonly used by quadcopter designs. Its motors and computation units are directly mounted to the tensegrity shell through custom-designed mounts. These parts are 3D printed with ONYX filament [37] for increased strength. Moreover, to evenly distribute weight, the design is powered by two batteries connected in series, with each battery attached to one of the horizontal rods of the shell (see Fig. 10). The design features a tension hook and an expanding end-cap for tension adjustment of the tensegrity (see Fig. 11). The hook allows for applying tension to individual strings, whereas the expanding end-cap can fine-tune the whole tension network by adjusting the distances between tensegrity nodes.

B. Collision resilience

We control the experimental vehicle to accelerate towards a concrete wall and collide with it to validate the vehicle's collision resilience. Notice that in this experiment, we take off the payload camera to better compare the experimental vehicle with its predecessor in [25], which has no payload and has survived a collision experiment with speed of 6.5m/s.

An image sequence from a high-speed video of a collision process is shown in Fig. 12. All parts within the tensegrity remain intact through the process. The vehicle also maintains its ability to fly after the collision. The experiment video is included in the attachment. We conduct ten collision tests like the one shown in the image sequence and summarize the results in Fig. 13. The green circles represent the cases in which the vehicle survives, whereas the red square represents the failure case. The experimental vehicle survives nine collisions, with the highest collision speed being 6.85m/s. For the

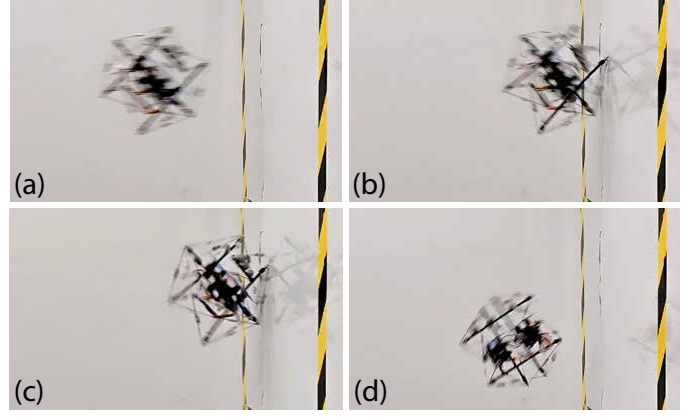


Figure 12. Image sequences of the process of a collision against a concrete wall: (a) Vehicle accelerates towards the wall. (b) Collision starts. (c) Vehicle comes to a full stop. (d) Vehicle bounces back from the wall. The speed of the vehicle right before this collision is 6.71m/s.

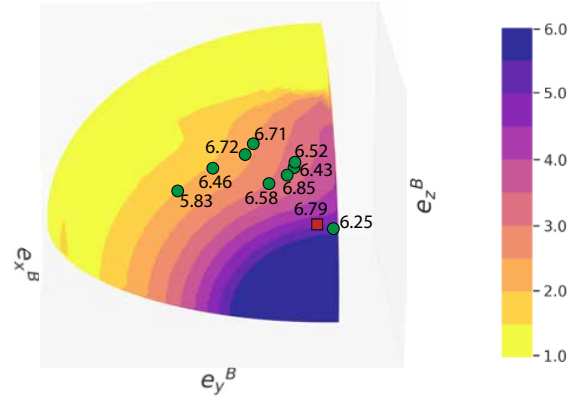


Figure 13. Result of the collision tests with the experimental tensegrity aerial vehicle. Each node shows the result of a single test. The node position represents the collision orientation with the relationship introduced in Section.II.B. The number near the node indicates the vehicle speed before the collision, in the unit of m/s. The node style denotes the collision result, green circle for survival and red square for failure. The octant surface color portrays the expected stress level based on the previous Monte Carlo study. For collisions of the same speed, darker color means worse stress concentration and a higher likelihood of failure. The value of the expected stress level of a given collision orientation is computed as the ratio of the maximum stress of that orientation to the smallest maximum stress of all possible orientations.

failure case, the collision speed is 6.79m/s and the vehicle hits the wall at an orientation that the Monte Carlo study predicts will lead to a large stress concentration. During the collision, the tensegrity shell fails as one of the 3D-printed end-cap shears. The result of the collision tests suggests that the experimental tensegrity aerial vehicle can survive high-speed impacts and our Monte Carlo study in Section. II provides a good intuition about the relationship between maximum stress in the tensegrity shell and the collision orientation.

C. Autonomous re-orientation

We also implement and validate the proposed re-orientation strategy with our experimental tensegrity vehicle. First, we generate the re-orientation path. When determining feasible rotations, we choose the coefficient of friction $\mu = 0.2$ for the non-sliding constraint, which accounts for friction between the

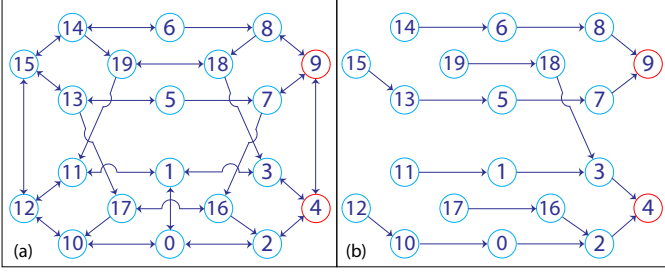


Figure 14. Process to generate a reorientation path. Each node represents a contact face and red nodes denote the goal faces the vehicle wish to rotate to. (a). We first generate a graph indicating all feasible rotations between faces. Each arrow indicates a feasible rotation. (b). We find the shortest paths for each face to rotate back to its closest goal face. Arrows indicate the directions of rotations between faces.

experimental vehicle and slippery surfaces like a wood floor. All feasible transitions for the experimental vehicle are shown in Fig. 14a and the generated re-orientation paths are in Fig. 14b, where the arrows indicate the rotation directions.

Moreover, we implement and evaluate the optimization-based torque-thrust converter in Section. III.D. When there is propeller thrust saturation, there will be an error between the torque commanded and the torque generated. We define the torque error rate as the ratio between the norm of the error and the norm of the command, and use it to evaluate the effectiveness of the thrust conversion. Here we use the rotation from face 3 to face 4 as an example for analysis because it requires a torque that simultaneously rolls, pitches, and yaws the vehicle. Moreover, it represents the most-traveled path on the re-orientation map. We compute the error rates for both the proposed optimization-based method and the pseudoinverse-clipping method, a widely-used strategy for quadcopter thrust conversion. The result is in Fig 15. Notice that when thrusts saturate, the error rate of the optimization-based method is about half of the pseudoinverse-clipping method. The smaller error rate suggests that the optimization-based thrust converter can help the vehicle better track re-orientation trajectories.

With the planned re-orientation path and the optimization-based thrust converter, we achieve a vehicle that can reliably re-orient and take off again. A video demonstrating this ability can be found in the attachment.

D. Autonomous operation in a forest environment

In previous experiments, we have tested the tensegrity aerial vehicle's collision resilience and re-orientation ability. In this experiment, we show how these abilities can be utilized to facilitate autonomous operation in a cluttered environment. Specifically, the experimental tensegrity aerial vehicle is commanded to move towards a goal in a previously-unknown forest with tree obstacles and uneven ground.

For this experiment, we use the extended Kalman filter (EKF) in [38] to estimate the state of the vehicle, which includes its position, velocity, and attitude. As we assume the vehicle operates in an environment with no external localization aid like GPS, motion-capture, or ultra-wide-band signals, we adopt the estimation strategy in [28], which reduces state estimation error by breaking a long flight to short hops and

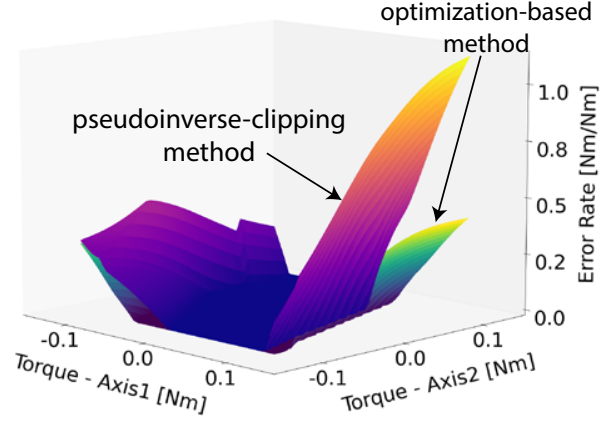


Figure 15. The surface plot shows the thrust conversion error rate for the rotation from face 3 to face 4. Axis 1 is the axis of the desired rotation and axis 2 points from the rotation point to the center of mass. The top surface is the error rate for the traditional method using pseudoinverse and clipping, whereas the bottom surface represents the error rate of the optimization-based method. Notice that the optimization-based method leads to a smaller error, and hence a better control result when thrust saturation takes place.

introducing pseudo zero-velocity measurements to the EKF when the vehicle's inertial sensor readings suggest that the vehicle is stationary.

If the experimental vehicle encounters a collision, indicated by the norm of the accelerometer reading exceeding a given threshold, a recovery controller will be triggered and the vehicle will mark the position where the collision occurs. The recovery controller increases the angular velocity control gains and commands a trajectory with a small constant negative velocity along the z-axis of the world frame, attempting to stabilize and land the vehicle softly. Once the vehicle has landed following a collision, it will re-orient itself and then attempt to hop around the obstacle it just collided with.

The experiments in this challenging outdoor environment expose some limits of the experimental vehicle. First, the navigation accuracy is limited by the accuracy and range of the inertial sensors. When a severe collision occurs, the accelerometer reading can saturate and this introduces a large error to the state estimator. Second, the re-orientation controller is limited by the torque authority of the vehicle and may fail when the vehicle rests on a large slope or gets trapped by a large indent on the ground. To mitigate these problems, we reduce hop speed to prevent fast collisions, and we command the vehicle to attempt backward hops if it is trapped.

A composite image of a test in the forest is shown in Fig. 16. In this experiment, the vehicle is ordered to move in a given direction for 3m and there is an unexpected tree obstacle between the start position and the goal position. During the experiment, a collision with the tree takes place during its second hop. The vehicle survives the collision, marks the position of the obstacle, hops sideways to avoid the obstacle, and then continues to hop toward the final goal position. A video of the experiment can be found in the attachment.

V. CONCLUSION

When an icosahedron tensegrity shell is under external loads, the loads will be distributed among the structural

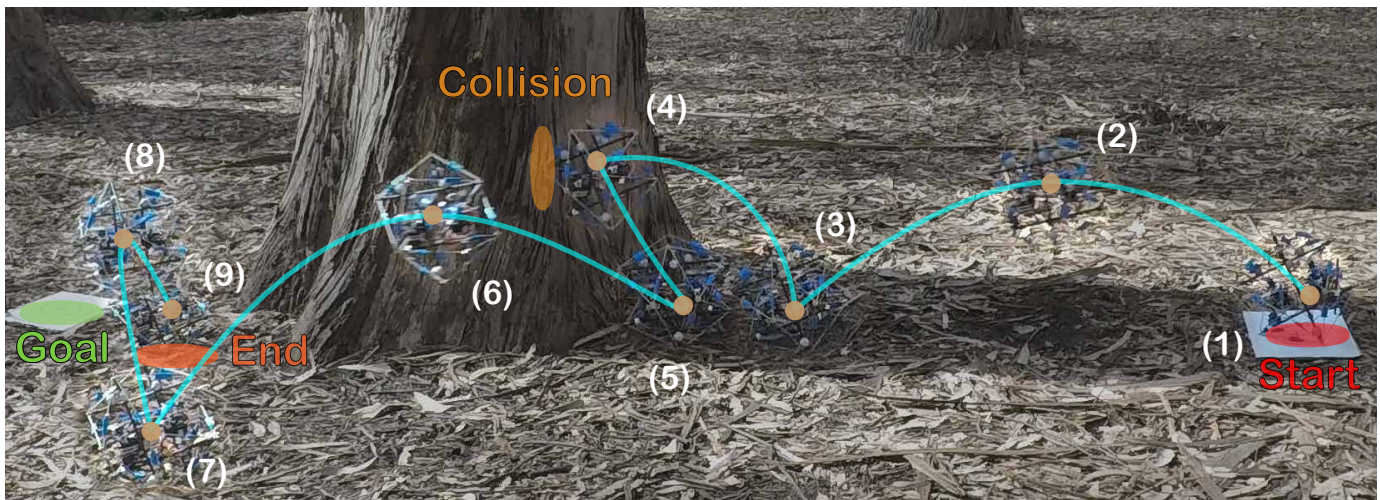


Figure 16. Composite image of the tensegrity aerial vehicle autonomously operating in a previously unknown forest environment. The cyan curve marks the movement of the vehicle. The vehicle is ordered to move from the start point on the right side of the figure to the goal point on the left. A tree obstacle exists between the two points. The vehicle successfully survives a collision with the tree and arrives at an endpoint close to the goal. The distance between the goal point and the end point is 0.25m. The background is desaturated to highlight the vehicle movement.

members as tension or compression, and the large stress concentration caused by bending is avoided. Utilizing this structural feature, we have created the tensegrity aerial vehicle, which is a collision-resilient aerial robot design with an icosahedron tensegrity structure. To guide the design process of the tensegrity aerial vehicles, we have devised a methodology that predicts the stresses in the structure during collisions with a dynamics simulation and selects components that can withstand the predicted stresses. With this methodology, we have successfully created an experimental vehicle with strong collision resilience that has survived a collision with a speed record of 6.85m/s. Meanwhile, we have created a re-orientation controller to help the tensegrity aerial vehicles take off again after collisions. Moreover, by adopting the strategy of replacing flight with short hops to mitigate the growth of state estimation error, the tensegrity aerial vehicles can carry out short-range autonomous operations without external sensors. The abilities to survive collisions, resume flight after collisions, and conduct short-range autonomous operations without external sensors allow the tensegrity aerial vehicles to work as field robots in areas with cluttered obstacles that are hard to detect and avoid.

ACKNOWLEDGEMENTS

The experimental testbed at the HiPeRLab is the result of contributions of many people, a full list of which can be found at hiperlab.berkeley.edu/members/. This work was supported by the UC Berkeley Fire Research Group, DARPA Subterranean Challenge and AI Institute for Next Generation Food Systems (AIFS). The authors would like to thank Alice Agogino, Alan Zhang and Douglas Hutchings for providing their insights on tensegrity design, and Joey Kroeger and Natalia Perez for their help in the development of the tensegrity aerial vehicle.

REFERENCES

- [1] S. Ramasamy, R. Sabatini, A. Gardi, and J. Liu, "Lidar obstacle warning and avoidance system for unmanned aerial vehicle sense-and-avoid," *Aerospace Science and Technology*, vol. 55, pp. 344–358, 2016.
- [2] N. Bucki, J. Lee, and M. W. Mueller, "Rectangular pyramid partitioning using integrated depth sensors (rappids): A fast planner for multicopter navigation," *IEEE Robotics and Automation Letters*, vol. 5, no. 3, pp. 4626–4633, 2020.
- [3] J. N. Yasin, S. A. S. Mohamed, M.-H. Hagbayan, J. Heikkonen, H. Tenhunen, and J. Plosila, "Unmanned aerial vehicles (UAVs): Collision avoidance systems and approaches," *IEEE Access*, vol. 8, pp. 105 139–105 155, 2020.
- [4] C. J. Salaan, K. Tadakuma, Y. Okada, Y. Sakai, K. Ohno, and S. Tadokoro, "Development and experimental validation of aerial vehicle with passive rotating shell on each rotor," *IEEE Robotics and Automation Letters*, vol. 4, no. 3, pp. 2568–2575, 2019.
- [5] VantageRobotics, "Vantage robotics - snap flying camera," <https://vantagerobotics.com>, (Accessed on 10/19/2019).
- [6] A. Briod, P. Kornatowski, J.-C. Zufferey, and D. Floreano, "A collision-resilient flying robot," *Journal of Field Robotics*, vol. 31, no. 4, pp. 496–509, 2014.
- [7] P. M. Kornatowski, S. Mintchev, and D. Floreano, "An origami-inspired resilience for multicopters," in *2017 IEEE/RSJ International Conference on Intelligent Robots and Systems (IROS)*. IEEE, 2017, pp. 6855–6862.
- [8] Flyability, "Elios 2," <https://www.flyability.com/elios-2>, (Accessed on 11/11/2019).
- [9] R. de Azambuja, H. Fouad, and G. Beltrame, "When being soft makes you tough: A collision resilient quadcopter inspired by arthropod exoskeletons," *arXiv preprint arXiv:2103.04423*, 2021.
- [10] H. Jia, S. Bai, R. Ding, J. Shu, Y. Deng, B. L. Khoo, and P. Chiraratananon, "A quadrotor with a passively reconfigurable airframe for hybrid terrestrial locomotion," *IEEE/ASME Transactions on Mechatronics*, pp. 1–11, 2022.
- [11] S. Mintchev, S. de Rivaz, and D. Floreano, "Insect-inspired mechanical resilience for multicopters," *IEEE Robotics and automation letters*, vol. 2, no. 3, pp. 1248–1255, 2017.
- [12] J. Jang, K. Cho, and G.-H. Yang, "Design and experimental study of dragonfly-inspired flexible blade to improve safety of drones," *IEEE Robotics and Automation Letters*, vol. 4, no. 4, pp. 4200–4207, 2019.
- [13] Z. Liu and K. Karydis, "Toward impact-resilient quadrotor design, collision characterization and recovery control to sustain flight after collisions," in *2021 IEEE International Conference on Robotics and Automation (ICRA)*. IEEE, 2021, pp. 183–189.
- [14] P. De Petris, H. Nguyen, M. Kulkarni, F. Mascarich, and K. Alexis, "Resilient collision-tolerant navigation in confined environments," in *2021 IEEE International Conference on Robotics and Automation (ICRA)*. IEEE, 2021, pp. 2286–2292.

- [15] M. Mote, M. Egerstedt, E. Feron, A. Bylard, and M. Pavone, "Collision-inclusive trajectory optimization for free-flying spacecraft," *Journal of Guidance, Control, and Dynamics*, vol. 43, no. 7, pp. 1247–1258, 2020.
- [16] J. Zha and M. W. Mueller, "Exploiting collisions for sampling-based multicopter motion planning," in *2021 IEEE International Conference on Robotics and Automation (ICRA)*, 2021, pp. 7943–7949.
- [17] H. Zhou, A. R. Plummer, and D. Cleaver, "Distributed actuation and control of a tensegrity-based morphing wing," *IEEE/ASME Transactions on Mechatronics*, vol. 27, no. 1, pp. 34–45, 2022.
- [18] J. J. Rimoli, "On the impact tolerance of tensegrity-based planetary landers," in *57th AIAA/ASCE/AHS/ASC Structures, Structural Dynamics, and Materials Conference*, 2016, p. 1511.
- [19] A. Zhang, D. Hutchings, M. Gupta, and A. Agogino, "Orientation control of self-righting tensegrity landers," in *International Design Engineering Technical Conferences and Computers and Information in Engineering Conference*, vol. 85451. American Society of Mechanical Engineers, 2021, p. V08BT08A025.
- [20] K. Garanger, I. del Valle, M. Rath, M. Krajewski, U. Raheja, M. Pavone, and J. J. Rimoli, "Soft tensegrity systems for planetary landing and exploration," *arXiv preprint arXiv:2003.10999*, 2020.
- [21] V. SunSpiral, G. Gorospe, J. Bruce, A. Iscen, G. Korbelt, S. Milam, A. Agogino, and D. Atkinson, "Tensegrity based probes for planetary exploration: Entry, descent and landing (edl) and surface mobility analysis," *International Journal of Planetary Probes*, vol. 7, p. 13, 2013.
- [22] K. Kim, L.-H. Chen, B. Cera, M. Daly, E. Zhu, J. Despois, A. K. Agogino, V. SunSpiral, and A. M. Agogino, "Hopping and rolling locomotion with spherical tensegrity robots," in *2016 IEEE/RSJ International Conference on Intelligent Robots and Systems (IROS)*. IEEE, 2016, pp. 4369–4376.
- [23] S. Mintchev, D. Zappetti, J. Willemin, and D. Floreano, "A soft robot for random exploration of terrestrial environments," in *2018 IEEE International Conference on Robotics and Automation (ICRA)*, 2018, pp. 7492–7497.
- [24] H. Cotgrove, "Tensegrity drones," <https://www.haydencotgrove.com/tensegrity-drones>, (Accessed on 01/02/2022).
- [25] J. Zha, X. Wu, J. Kroeger, N. Perez, and M. W. Mueller, "A collision-resilient aerial vehicle with icosahedron tensegrity structure," in *2020 IEEE/RSJ International Conference on Intelligent Robots and Systems (IROS)*. IEEE, 2020, pp. 1407–1412.
- [26] R. Fedorenko, "Tensodrone that do not break, and what does architecture, robotic manipulator and copter have in..." Aug 2020. [Online]. Available: <https://medium.com/@frontwise/tensodrone-2ddc18bce6a9>
- [27] S. Savin, A. Al Badr, D. Devitt, R. Fedorenko, and A. Klimchik, "Mixed-integer-based path and morphing planning for a tensegrity drone," *Applied Sciences*, vol. 12, no. 11, p. 5588, 2022.
- [28] X. Wu and M. W. Mueller, "Using multiple short hops for multicopter navigation with only inertial sensors," in *2020 IEEE International Conference on Robotics and Automation (ICRA)*. IEEE, 2020, pp. 8559–8565.
- [29] M. W. Mueller, M. Hehn, and R. D'Andrea, "A computationally efficient motion primitive for quadcopter trajectory generation," *IEEE transactions on robotics*, vol. 31, no. 6, pp. 1294–1310, 2015.
- [30] B. Jessen, "Orthogonal icosahedra," *Nordisk Matematisk Tidskrift*, pp. 90–96, 1967.
- [31] S. Pellegrino and C. R. Calladine, "Matrix analysis of statically and kinematically indeterminate frameworks," *International Journal of Solids and Structures*, vol. 22, no. 4, pp. 409–428, 1986.
- [32] F. Beer, E. Johnston, J. DeWolf, and D. Mazurek, "Mechanics of materials. 7th edition," *New York. McGraw-Hill Education Ltd*, 2015.
- [33] R. Goyal and R. E. Skelton, "Dynamics of class 1 tensegrity systems including cable mass," in *16th biennial ASCE international conference on engineering, science, construction and operations in challenging environments*, 2018.
- [34] R. Fenwick and D. Bull, "What is the stiffness of reinforced concrete walls," *SESOJ journal*, vol. 13, no. 2, pp. 23–32, 2000.
- [35] A. P. Boresi, R. J. Schmidt, O. M. Sidebottom *et al.*, *Advanced mechanics of materials*. Wiley New York, 1985, vol. 6.
- [36] J. Mattingley and S. Boyd, "Cvxgen: A code generator for embedded convex optimization," *Optimization and Engineering*, vol. 13, no. 1, pp. 1–27, 2012.
- [37] MarkForged. (2021) Onyx. [Online]. Available: <https://markforged.com/materials/plastics/onyx>
- [38] M. W. Mueller, M. Hehn, and R. D'Andrea, "Covariance correction step for kalman filtering with an attitude," *Journal of Guidance, Control, and Dynamics*, vol. 40, no. 9, pp. 2301–2306, 2017.



Jiaming Zha received his bachelor of science degree from Rice University, USA in 2018 and master of science degree from University of California, Berkeley, USA in 2020. He is currently a Ph.D. candidate at the High Performance Robotics Lab at UC Berkeley. His research interests are novel mechanical design, control and path planning for aerial vehicles.



Xiangyu Wu received his bachelor of science degree from Beijing Institute of Technology, China in 2017. He received his master of science degree in 2019 and his Ph.D. degree in 2022, both from University of California, Berkeley, USA. His research interests are the state estimation and path planning of multi-copters.



Ryan Dimick received his bachelor of science degree from University of California, Davis, USA in 2017 and master of science degree from University of California, Berkeley, USA in 2021. He is currently a robotics software engineer at Dusty Robotics.



Mark W. Mueller is an assistant professor of Mechanical Engineering at the University of California, Berkeley, and runs the High Performance Robotics Laboratory (HiPeRLab). He received a Dr.Sc. and M.Sc. from the ETH Zurich in 2015 and 2011, respectively, and a BSc from the University of Pretoria in 2008. His research interests include aerial robotics, their design and control, and especially the interactions between physical design and algorithms.